

Light emission from a scanning tunneling microscope: Fully retarded calculation

Peter Johansson*

Department of Theoretical Physics, University of Lund, Sölvegatan 14 A, S-223 62 Lund, Sweden
(April 30, 2018)

The light emission rate from a scanning tunneling microscope (STM) scanning a noble metal surface is calculated taking retardation effects into account. As in our previous, non-retarded theory [Johansson, Monreal, and Apell, Phys. Rev. B **42**, 9210 (1990)], the STM tip is modeled by a sphere, and the dielectric properties of tip and sample are described by experimentally measured dielectric functions. The calculations are based on exact diffraction theory through the vector equivalent of the Kirchoff integral. The present results are qualitatively similar to those of the non-retarded calculations. The light emission spectra have pronounced resonance peaks due to the formation of a tip-induced plasmon mode localized to the cavity between the tip and the sample. At a quantitative level, the effects of retardation are rather small as long as the sample material is Au or Cu, and the tip consists of W or Ir. However, for Ag samples, in which the resistive losses are smaller, the inclusion of retardation effects in the calculation leads to larger changes: the resonance energy decreases by 0.2–0.3 eV, and the resonance broadens. These changes improve the agreement with experiment. For a Ag sample and an Ir tip, the quantum efficiency is $\approx 10^{-4}$ emitted photons in the visible frequency range per tunneling electron. A study of the energy dissipation into the tip and sample shows that in total about 1 % of the electrons undergo inelastic processes while tunneling.

PACS numbers: 61.16.Ch, 41.20.Bt, 73.20.Mf, 78.20.Bh

I. INTRODUCTION

The scanning tunneling microscope (STM) has over the last 15 years developed into a standard instrument in surface science. A relatively small, but very interesting part of this development is concerned with light emission from STM's. This phenomenon, in which the tunneling electron transfers energy to a photon,¹ has been observed on noble-metal surfaces by Gimzewski, Berndt, and co-workers,^{2–6} and later by several other groups.^{7–11} Light emission was also observed from semiconductors,^{12–15} from surfaces covered by molecules,¹⁶ and from magnetic surfaces.¹⁷ Other experiments have studied closely related phenomena. To mention a few examples, the STM tip can be used as a local detector of photoelectrons in photoemission,¹⁸ and if the STM is illuminated by laser light, the rectification current can be large enough to generate STM topographs.¹⁹ Moreover, the interaction between propagating surface plasmons and an STM tip has been investigated.²⁰

Light emission from noble-metal surfaces has inspired a certain amount of theoretical activity.^{21–27} The most striking experimental results, the high (in this context) quantum efficiency of the process (up to 10^{-3} photons per electron) and the characteristic resonances in the light emission spectra, can be understood in the following way:^{21–29} When the tip-sample separation is no more than 5–10 Å, the surface plasmons on the two surfaces interact quite strongly and form an interface-plasmon mode. This is illustrated schematically in Fig. 1. The resonance in the light emission spectrum occurs at the frequency for which half a wavelength of the interface mode fits into the “cavity” between tip and sample. The charge oscillations associated with the interface plasmon

have opposite signs on the two electrodes. This has two major consequences: (i) The charge on one surface gives a field that polarizes the second surface so that the polarizing field at the first surface increases, etc. Thus, given the charge configuration of the interface mode, the enhancement of the electromagnetic vacuum fluctuations is a quite natural consequence. (ii) Because the charges on the tip and the sample are opposite, the interface plasmon is locally charge-neutral. This weakens the restoring forces compared with the case of a surface plasmon at an isolated interface, and the resonance peak is red-shifted relative to the surface plasma frequency. From this argument follows also a geometry-dependence of the resonance frequency. A larger tip radius and a smaller tip-sample separation gives a more red-shifted resonance.

Model calculations based on the physical picture described above gave results in rather good agreement with experiment, both in terms of absolute intensities and spectral properties. In these calculations, the complicated, extended geometrical shape of the STM tip was approximated by a sphere, and the electromagnetic field near the model tip was calculated in the non-retarded limit.^{21,22} The justification for the approximations is that the region *between* the tip and sample is most important for the effect. There the tip shape is well approximated by a sphere, and all relevant distances are small compared with the wavelength of the emitted photons.

However, in view of future developments, it is rather useful to know how good these approximations are. In this paper, we focus on the effects of retardation. The calculations are built on exact diffraction theory, and leads to equations that can be solved numerically with good accuracy without too much effort.

A number of calculations have addressed related

problems.^{30–34} One example of this is scanning near-field optical microscopy (SNOM),^{30,31,35} where one studies *photon* tunneling from a transparent sample to a tip. The tip-sample distance may be several hundred Å in this case, so it becomes necessary to take retardation into account. But the calculations can often be carried out using various discretization schemes in real space,³² since the relevant length scales differ by at most an order of magnitude. It deserves to be pointed out that the calculational scheme developed in this paper could, with some extensions, also be applied to SNOM problems, and may then be faster than the prevailing methods. However, a prerequisite for this is that the tip-sample geometry possesses some (preferably cylindrical) symmetry.

In another fully retarded calculation, Takemori, Inoue, and Ohtaka³³ (TIO) studied the field around a sphere in front of a plane surface with the aim of investigating electromagnetic effects in surface-enhanced Raman scattering (SERS).³⁶ Finally, Madrazo, Nieto-Vesperinas, and Garcia²⁶ (MNVG) have considered light emission from an STM in a calculation accounting for retardation. They used an essentially two-dimensional (2D) model geometry, where the tip was represented by a horizontal cylinder and the sample surface was artificially corrugated. We will compare our results with those of MNVG in as far as this is possible (they presented results for one single photon energy) and we will see that the different model geometries lead to quite different results.

The inclusion of retardation effects does not change the basic picture of how light is emitted from an STM, however, at a quantitative level, there are changes to some of the calculated results. As a general observation, retardation effects become increasingly important when the tip and/or sample materials are good conductors (such as silver). Then the energy dissipation in the near-field zone is rather small, and a localized mode will instead be damped because some energy propagates away from the near-zone. This is of course allowed for in a retarded, but not in a non-retarded, calculation. Thus for a Ag sample scanned by a Ir or W tip, retardation leads to an additional red-shift of the resonance frequency, and this improves the agreement between theory and experiment. For Au and Cu samples, on the other hand, the resonance frequency is essentially unchanged, and there are only relatively minor changes of the light emission intensity as a result of retardation effects.

The rest of the paper is organized as follows: In Sec. II, we develop the formalism needed to carry out a retarded calculation of the electromagnetic field that results from inelastic tunneling. We derive expressions for the radiated power, as well as the power dissipated in the sample and tip. In Sec. III, we establish the connection between the completely classical current we use in the electrodynamic calculations, and the transition matrix elements associated with inelastic tunneling of an electron from the tip to the sample or vice versa. The numerical results of our calculation are presented in Sec. IV, and compared with experimental results. Finally, our conclusions are

presented in Sec. V.

II. THE ELECTROMAGNETIC FIELD CALCULATION

A. General considerations

We will calculate the electromagnetic field resulting from excitation by a *classical* current distribution $\mathbf{j}_e(\mathbf{r})e^{-i\omega t}$, localized between the tip and the sample. As in our previous, non-retarded calculations, we model the tip by a sphere with radius R that is centered at the origin of our coordinate system, see Fig. 1. The sample fills the half-space $z < z_0$, where $z_0 = -(d + R)$, d being the tip-sample separation.

The optical properties of the tip and sample materials are described by local dielectric functions $\epsilon_1(\omega)$ (sample) and $\epsilon_2(\omega)$ (tip) determined from experiment.³⁷ While this is an approximation, it is a reasonable one; we will discuss its limitations in some more detail in Sec. IV D.

We write the source current distribution as

$$\mathbf{j}_e(\mathbf{r}) = \hat{z}F(\rho)\delta(z - z_0)C. \quad (1)$$

The source is in other words a cylindrically symmetric dipole layer right at the sample surface. Most of the time we will take the radial form factor $F(\rho)$ to be a Gaussian

$$F(\rho) = e^{-\rho^2/a^2} \quad (2)$$

with $a \sim 5 \text{ \AA}$ (as long as the current is concentrated to a region near the symmetry axis the exact shape of $F(\rho)$ is unimportant). Even if we treat \mathbf{j}_e as a classical current, its strength C , must eventually be determined from a quantum-mechanical calculation, which we defer to Sec. III.

Thanks to the cylindrical symmetry of both the current distribution and the tip and the sample, the magnetic flux density is always directed along the azimuthal unit vector $\hat{\phi}$, and its magnitude only depends on z and the distance ρ , to the cylindrical symmetry axis,

$$\mathbf{B}(\mathbf{r}) = B(\rho, z)\hat{\phi}. \quad (3)$$

The accompanying \mathbf{E} field is also cylindrically symmetric. In the region between the tip and the sample, it is mainly directed along \hat{z} and thus strongly coupled to \mathbf{j}_e . Applying Maxwell's equations, we find that \mathbf{B} must satisfy the vector Helmholtz equation (we use SI units and μ_0 is the vacuum permeability)

$$\nabla^2 \mathbf{B} + k_i^2 \mathbf{B} = -\mu_0 \nabla \times \mathbf{j}_e \quad (4)$$

in each of the three different regions of space. In vacuum $k_0^2 = k^2 = \omega^2/c^2$, in the sample $k_1^2 = \epsilon_1(\omega)k^2$, and in the sphere $k_2^2 = \epsilon_2(\omega)k^2$. Inside the sphere the solution to Eq. (4) can be written

$$\mathbf{B} = \hat{\phi} \sum_{l=1}^{\infty} a_l \frac{j_l(k_2 r)}{j_l(k_2 R)} P_l^1(\cos \theta), \quad (5)$$

where r , θ , and ϕ are the usual spherical coordinates, j_l is a spherical Bessel function, P_l^1 is an associated Legendre function, and a_l is a set of coefficients that remain to be determined. In the sample we write \mathbf{B} as a Fourier-Bessel transform,

$$\mathbf{B} = \hat{\phi} \int_0^{\infty} \kappa d\kappa B(\kappa) J_1(\kappa \rho) \times \exp \left[-i \sqrt{k_1^2 - \kappa^2} (z - z_0) \right], \quad (6)$$

where J_1 is an ordinary Bessel function, while $B(\kappa)$ is an as yet unknown function. Equation (5) yields a finite field at the center of the sphere, Eq. (6) gives outgoing, damped waves in the sample, and both expressions satisfy Eq. (4). Next we must determine a_l and $B(\kappa)$.

B. The solution

To calculate the field in the vacuum region, we use the vector equivalent of the Kirchoff integral³⁸

$$\mathbf{B}(\mathbf{r}) = \mathbf{B}^{(e)}(\mathbf{r}) + \int dS' [(\hat{n}' \times \mathbf{B}(\mathbf{r}')) \times \nabla' G - \frac{ik}{c} G(\hat{n}' \times \mathbf{E}(\mathbf{r}'))]. \quad (7)$$

Here, the first term $\mathbf{B}^{(e)}$ solves Eq. (4) when neither the sample nor the tip is present, i.e., it yields the direct contribution to \mathbf{B} from the source. G stands for the Green's function to the scalar Helmholtz equation in vacuum,

$$G(\mathbf{r}, \mathbf{r}') = \frac{e^{ik|\mathbf{r}-\mathbf{r}'|}}{4\pi|\mathbf{r}-\mathbf{r}'|}. \quad (8)$$

The integration dS' in Eq. (7) runs over two surfaces: a plane just outside the sample and a spherical surface just outside the model tip. The normal vector \hat{n}' points in the direction from the sphere or half-space into the vacuum region. The fields $\mathbf{B}(\mathbf{r}')$ and $\mathbf{E}(\mathbf{r}')$ are the exact fields on the two surfaces, so Eq. (7) is an integral equation.

Before continuing, let us point out that even if the surface integral in Eq. (7) contains the full \mathbf{B} and \mathbf{E} fields on the surfaces, the combination appearing in the integral guarantees that the final result only contains reflected waves. If one for example wants to calculate the field from a certain source distribution in vacuum, but nevertheless introduces a surface somewhere outside the source, the integral does not at all contribute to $\mathbf{B}(\mathbf{r})$. In the present case, the integral over the spherical surface vanishes if $\epsilon_2 = 1$, and the integral over the flat surface vanishes if $\epsilon_1 = 1$.

Since Eq. (7) yields the field \mathbf{B} at any point outside the tip and sample, it can be used to find expressions

determining a_l and $B(\kappa)$. Just outside the surfaces over which we integrate, we can (i) either calculate the field from Eq. (7), or (ii) we can use Eq. (5) or Eq. (6) because \mathbf{B} is continuous across the interfaces. The so obtained, different expressions for \mathbf{B} must be equal. Expanding the result outside the sphere in terms of associated Legendre functions yields

$$a_l = a_l^{(e)} + s_l a_l + \int_0^{\infty} \kappa d\kappa f_l(\kappa) B(\kappa), \quad (9)$$

where $a_l^{(e)}$ comes directly from the source, the term $s_l a_l$ comes from the integration over the sphere, and the last term originates from the sample surface integration. Without the sample, the above equation has the solution $a_l = a_l^{(e)}/(1 - s_l)$; thus, plasmon resonances occur on the isolated sphere when $s_l = 1$. The corresponding equation, valid at the sample surface, is

$$B(\kappa) = B^{(e)}(\kappa) + S(\kappa)B(\kappa) + \sum_{l=1}^{\infty} a_l g_l(\kappa). \quad (10)$$

Removing the sphere, $B(\kappa) = B^{(e)}(\kappa)/(1 - S(\kappa))$, so the surface plasmon resonances occur when $S(\kappa) = 1$. The explicit expressions for $B^{(e)}(\kappa)$, $f_l(\kappa)$, $g_l(\kappa)$, s_l , $S(\kappa)$, $a_l^{(e)}$, and $a_l^{(p)}$ are given below and in the Appendix.

To solve for a_l and $B(\kappa)$, we first note that Eq. (10) has the formal solution

$$B(\kappa) = \frac{B^{(e)}(\kappa) + \sum_{l=1}^{\infty} a_l g_l(\kappa)}{1 - S(\kappa)}. \quad (11)$$

Inserted into Eq. (9) this yields a system of linear equations determining the coefficients a_l ,

$$[1 - s_l]a_l - \sum_{l'=1}^{\infty} M_{ll'} a_{l'} = a_l^{(e)} + a_l^{(p)}, \quad (12)$$

where

$$M_{ll'} = \int_0^{\infty} \kappa d\kappa \frac{f_l(\kappa) g_{l'}(\kappa)}{1 - S(\kappa)}. \quad (13)$$

The terms on the right hand side are the driving forces and depend on the source: $a_l^{(e)}$ is the direct contribution from the source, while $a_l^{(p)}$ results from the source fields reflected *once* off the sample surface. The two coefficients can be added together to give

$$a_l^{(e)} + a_l^{(p)} = \int_0^{\infty} \kappa d\kappa \frac{f_l(\kappa) B^{(e)}(\kappa)}{S(\kappa)[1 - S(\kappa)]}. \quad (14)$$

$B^{(e)}(\kappa)$ is the Fourier-Bessel transform of the solution to Eq. (4) at $z = z_0$ and with $\epsilon_1 = 1$ and $\epsilon_2 = 1$. Using the expression in Eq. (A1) for the Green's function, we get

$$\begin{aligned} B^{(e)}(\kappa) &= \frac{-i\mu_0 C}{2\sqrt{k^2 - \kappa^2}} \int_0^{\infty} \rho d\rho F'(\rho) J_1(\kappa \rho) = \\ &= \frac{i\mu_0 C}{\sqrt{k^2 - \kappa^2}} \frac{\kappa a^2}{4} e^{-\kappa^2 a^2/4}, \end{aligned} \quad (15)$$

where the second line is valid if $F(\rho)$ is given by Eq. (2).

To summarize, a numerical calculation of the electromagnetic field begins by evaluating s_l , M_{ll} , and $a_l^{(e)} + a_l^{(p)}$ from the formulas given here and in the Appendix. Then the coefficients a_l can be found by a matrix inversion in Eq. (12). Having found a_l , we get $B(\kappa)$ from Eq. (11), and subsequently $\mathbf{B}(\mathbf{r})$ can be calculated anywhere in space. These steps must of course be repeated for each photon frequency ω .

To carry out the matrix inversion in practice, a truncation in l at l_{\max} must be introduced. With the geometry parameters that we consider most of the time ($d \sim 5 \text{ \AA}$, and $R \lesssim 500 \text{ \AA}$), $l_{\max} \sim 50$ is appropriate in order to get converged results. l_{\max} is determined by the size of the resonant cavity between the tip and the sample. The interface-plasmon mode is to a large extent confined within the region where the distance between tip and sample is less than twice the *smallest* tip-sample separation d (cf. Ref. 28). For a spherical tip this region has a radius $\sqrt{2dR}$ (if $d \ll R$), i.e., with $d = 5 \text{ \AA}$ and $R = 300 \text{ \AA}$ we get a ‘‘plasmon radius’’ of $\approx 55 \text{ \AA}$. Since $\pi R \approx 950 \text{ \AA}$, it is clear that even a crude description of the interface plasmon would require $l_{\max} \sim 20$, but to capture its structure a large number of basis functions is needed.

The computation of the radiated power for one frequency takes less than 5 seconds on an ordinary work station. Most of this time is used for the κ integration determining M_{ll} in Eq. (13).

C. Emitted power

Once the coefficients a_l have been determined, we can evaluate the radiation power as well as the power dissipated into the sample and tip. In vacuum, far from the model tip, the \mathbf{B} field has the asymptotic behavior

$$\mathbf{B} = \hat{\phi} B_{\text{far}} \frac{e^{ikr}}{r}. \quad (16)$$

B_{far} is a sum of contributions from the source, the sample surface, and the spherical surface,

$$B_{\text{far}} = -[1 + S(k \sin \theta)] k \cos \theta B(k \sin \theta) e^{ik(d+R) \cos \theta} - \sum_{l=1}^{\infty} a_l \frac{e^{-il\pi/2}}{k} \sqrt{\frac{2l+1}{4\pi}} P_l^1(\cos \theta) \frac{s_l}{h_l(kR)}. \quad (17)$$

Knowing B_{far} , we can calculate the radiated (differential) power per unit solid angle

$$\frac{dP_{\text{rad}}}{d\Omega} = \frac{1}{2} c^3 \epsilon_0 |B_{\text{far}}|^2. \quad (18)$$

By evaluating the Poynting vector on the surface of the model tip and then taking the time average, we find that the power dissipated into the sphere is given by

$$P_{\text{sph}} = \pi R^2 \frac{c^3 \epsilon_0}{k} \times \sum_{l=1}^{\infty} \frac{2l(l+1)}{2l+1} |a_l|^2 \text{Im} \left[-\frac{1}{\epsilon_2} \left(\frac{1}{R} + k_2 \frac{j_l'(k_2 R)}{j_l(k_2 R)} \right) \right]. \quad (19)$$

A similar calculation yields the power absorbed in the sample

$$P_{\text{samp}} = \pi \frac{c^3 \epsilon_0}{k} \int_0^{\infty} \kappa d\kappa |B(\kappa)|^2 \text{Re} \left[\frac{\sqrt{k_1^2 - \kappa^2}}{\epsilon_1} \right]. \quad (20)$$

D. Comparison with other methods

Takemori, Inoue, and Ohtaka³³ studied scattering of a plane wave impinging on a sphere-plane system. This problem can be studied also in the present framework if $\mathbf{B}^{(e)}$ is taken to describe the incoming wave. Of course, the solution would not in general be restricted to cylindrically symmetric electric multipole modes as is the case here, but thanks to the cylindrical symmetry there would not be any mixing of modes with different m . The numerical solution would therefore be quite feasible. Note also that thanks to the reciprocity theorem,³⁹ already the present calculation can yield results for the z component of the electric field induced by an incoming wave on the cylindrical symmetry axis below the tip.

The conversion of plane waves to spherical waves and vice versa is central to both our solution and that of TIO. However, the conversion is dealt with in different ways. TIO essentially sum up the contributions from repeated scattering, back and forth, between the sphere and the plane. These repeated scattering events are implicitly included in the Kirchoff integral formulation. Thus, we feel that, at least once the field has been written in the form of Eq. (7), the present solution is conceptually simpler.

Our calculation and the one by Madrazo, Nieto-Vesperinas, and Garcia^{26,40} have similar starting points; in both cases the electromagnetic field is expressed in terms of integrals over the surfaces where the relative dielectric function changes in a discontinuous way. However, unlike us, MNVG choose to solve the resulting integral equations in real space. While MNVG treat a situation where the sample surface is periodically corrugated, it seems like their method would require quite intensive numerical calculations even for the case of a flat sample.

III. THE SOURCE

In order to perform the explicit calculations, we need to specify the sources. The tunnel current of an STM is typically concentrated to a small area; most of the current goes through the very last atom at the end of the tip. Also the inelastic transitions, from a state in one of

the electrodes to a lower-energy state in the other electrode, that drive the light emission are concentrated to the same small region of space.

We wish to relate the classical ac current \mathbf{j}_e in Eq. (1) to quantum-mechanical transition matrix elements. Let us first look at one particular electronic transition from the state $|i\rangle$ to $|f\rangle$. The corresponding classical current is⁴¹

$$\mathbf{j}_e^{(fi)}(\mathbf{r}) = \langle f|2\mathbf{j}(\mathbf{r})|i\rangle. \quad (21)$$

The resulting current distribution is of course not identical to that of Eqs. (1) and (2), however, the current is mainly directed along \hat{z} and it is concentrated to a small region near the end of the tip. As a consequence, the two current distributions generate essentially the same fields provided their dipole moments

$$\int d^3r z \rho_e(\mathbf{r}) \quad \text{and} \quad \int d^3r z \rho_e^{(fi)}(\mathbf{r})$$

are equal. Here the charge distributions ρ_e and $\rho_e^{(fi)}$ are connected to \mathbf{j}_e and $\mathbf{j}_e^{(fi)}$ through continuity equations such as

$$\frac{\partial \rho_e}{\partial t} + \nabla \cdot \mathbf{j}_e = 0. \quad (22)$$

In order for the dipole moments to be equal, we must have

$$-\frac{2\pi C_{fi}}{i\omega} \int_0^\infty \rho d\rho F(\rho) = -\frac{1}{i\omega} \int d^3r \langle f|2j_z(\mathbf{r})|i\rangle. \quad (23)$$

Here C_{fi} is the value C would take if $(|i\rangle \rightarrow |f\rangle)$ was the only inelastic transition contributing to photon emission.

In the experiment, light emission is caused by many different transitions at a whole range of frequencies. Therefore the factor C entering Eq. (1) should be an *incoherent sum* of the different C_{fi} ; moreover, we should calculate the emitted power *per unit photon energy* rather than just the emitted power. All the expressions for radiated or dissipated power found from (Eqs. (18), (19), and (20)) are proportional to $|C|^2$. We need to replace $|C|^2$ by a new quantity, $|\mathcal{C}|^2(\omega)$, in order to get expressions for the radiated or dissipated power per unit photon energy. For the transitions around photon energy $\hbar\omega$, we have

$$|\mathcal{C}|^2(\omega) = \sum_{fi} |C_{fi}|^2 \delta(E_i - E_f - \hbar\omega). \quad (24)$$

With the aid of Eq. (23), this can be rewritten as

$$|\mathcal{C}|^2(\omega) = \sum_{fi} \frac{|\langle f|2j_z|i\rangle|^2}{4\pi^2 |\int_0^\infty \rho d\rho F(\rho)|^2} \delta(E_i - E_f - \hbar\omega). \quad (25)$$

Now, for example, the radiated power per unit solid angle and photon energy is

$$\frac{dP_{rad}}{d(\hbar\omega)d\Omega} = \frac{|\mathcal{C}|^2(\omega)}{|C|^2} \frac{1}{2} c^3 \epsilon_0 |B_{far}|^2 \quad (26)$$

if the calculation of B_{far} is still based on a source described by Eq. (1).

In the actual calculation of $|\mathcal{C}|^2(\omega)$, we have used free-electron models for both the tip and sample; more details can be found in Ref. 22. The resulting $|\mathcal{C}|^2$ is rather featureless; the ω dependence is roughly

$$|\mathcal{C}|^2(\omega) \propto \left(1 - \frac{\hbar\omega}{eV_{bias}}\right), \quad (27)$$

where V_{bias} is the bias voltage. We have not tried to improve on these earlier calculations, for the effects we are mainly interested in are of electrodynamic origin.⁴²

We should point out that we restricted the evaluation of the transition matrix elements to the vacuum (barrier) region. There are several good reasons for doing that: Since, in the frequency range where the photon emission is most intense, $|\epsilon_{tip}|$ and $|\epsilon_{sample}|$ are considerably larger than 1, the electric field that couples to the tunnel current is stronger in the vacuum region. Moreover, the electron wave functions oscillate inside the sample and tip, whereas they do not change sign in the barrier region. This means that the vacuum region should give the largest contributions to the matrix elements.

Persson and Baratoff²³ studied this issue rather thoroughly by comparing the contributions to photon emission from inelastic tunneling and hot-electron decay. Within their model, in which electrons are tunneling into a spherical metal particle, inelastic tunneling processes (light emission while the electron is in the barrier) are about 3 orders of magnitude more effective than hot-electron decay (light emission when the electron has reached the final-state electrode) in the light-emission process.

IV. RESULTS

We have calculated the electromagnetic field for a number of different materials combinations and geometric parameters. Below we present results for the differential power (i.e. the radiated power per unit solid angle and photon energy) and the total radiated or dissipated power per unit photon energy.

When we present results for the differential power, we take the observation angle to be $\theta = 57.3^\circ$ (i.e. 1 rad). The angular distribution of radiation shows only slight variations with frequency, materials, etc. It is given by a dipolar radiation lobe that has been “turned” away from $\theta=90^\circ$ to have a maximum at $\theta=55-60^\circ$. Very similar angular distributions show up both in experiments (Fig. 30 of Ref. 43) and other calculations (see Refs. 24 and 33).

A. Au sample—W tip

We begin by considering light emission from a Au sample probed by a W tip. Figure 2 presents results for the differential power from both retarded and non-retarded calculations. As for the spectral shape, these results should be directly comparable with experiment (typically photons are collected over a certain solid angle in the experiments).⁴ Here, retardation does not cause any qualitative changes of the spectra. For a tip radius $R=100$ Å, the retarded and non-retarded results cannot be distinguished from each other. When R is increased to 300 Å, there is a difference in terms of intensity between the retarded and non-retarded results, but the spectral shape and resonance frequency is nearly the same. These spectra are in quite good agreement with the experimental ones.⁴

When the sample consists of Au (and the same holds true for Cu), the resonance frequency is not very sensitive to the tip-sample geometry. The reason is that, because of the onset of interband transitions, the real part of the dielectric function ϵ_{Au} increases very rapidly from ≈ -11 at 2 eV to ≈ -2 at 2.5 eV. Thus, even though changes in the geometry leads to changes in the resonance condition expressed in terms of a value for the sample dielectric function, the resonance frequency does not change much; here there is only a slight red-shift of the resonance when R increases from 100 to 300 Å.

Umeno *et al.*¹⁰ observed light emission from a granular Au film, and found variations in the resonance frequency that they interpreted as the result of a varying tip curvature. That interpretation is in qualitative agreement with our results, but a quantitative comparison is not possible for at least two reasons: (i) In its present form, our theory does not account for the granularity of the film. (ii) The bias voltage was as low as 2 V in the experiment, so the resonance frequency was most likely limited by V_{bias} . It would be interesting to see the experiment repeated at a larger bias.

B. Ag sample—Ir tip

Next let us look at the radiation spectra from a silver sample scanned by an Ir tip. In Fig. 3 we display results of calculations including retardation with three different tip radii (200, 300, and 400 Å, respectively), and for comparison also results from a non-retarded calculation with $R=300$ Å. Here, the retarded and non-retarded results still have the same basic features, but the inclusion of retardation effects leads to substantial changes at the quantitative level. The primary resonance frequency is red-shifted, the second peak (between 3 and 3.5 eV) reduces to a shoulder, the peak height is reduced by almost a factor of 2, and the peak becomes broader.

One important reason for the lowering of the resonance frequency and increased damping (width) of the reso-

nance appears to be that the fields penetrate further into the sample and tip when retardation effects are included in the calculation. This increases the resistive losses suffered by the tip-induced plasmon mode. We would like to stress that radiation damping as such plays *no* role in broadening the resonance here; as we will see below, the radiated power is just a small fraction of the dissipated power.

The changes brought about by the retardation effects improve the agreement between calculated and experimental spectra. The second peak, seen in the non-retarded calculation but not in experiment, is gone, and the extra red-shift found in the retarded calculation brings the remaining resonance closer to its experimental position (typically 2.5 eV).³ At the same time, a word of caution is in place here. The calculated spectra are clearly quite sensitive to the tip-sample geometry. In experiments, the peak positions varied somewhat between spectra taken with different tips on silver samples.⁴ However, these variations were not as large as those seen in Fig. 3, where the resonance frequency is lowered by ≈ 0.5 eV when R is increased from 200 Å to 400 Å. Unfortunately, our limited knowledge about the actual shape of the STM tip makes it difficult to reach any definite conclusion about this issue.

Further insight can be gained by studying how the total radiated power, as well as the power lost to the tip and sample, vary with frequency. Such results are displayed in Fig. 4 for the case of a Ag sample and an Ir tip with $R=300$ Å. The losses to the tip and sample are much larger than the radiated power (note that the P_{rad} data are multiplied by a factor of 100). From the figure, the *total* radiated power can be estimated to

$$25 \times 10^6 \frac{\text{W}}{\text{J}} \times 1\text{eV} \approx 4pW,$$

or 10^7 photons/sec. The tunnel current 10 nA corresponds to $\approx 0.62 \times 10^{11}$ tunneling electrons per second. Thus, the quantum efficiency is about 2×10^{-4} photons/tunneling electron. This is in reasonable agreement both with the results of our earlier calculations^{21,22} and experimental estimates.^{3,4}

Here one should note that the electromagnetic response is not always the limiting factor for the quantum efficiency. To reach the values found above, the bias voltage must be 1 V, or so, larger than the resonance photon energy. But if the bias voltage is just 2 V, and in addition a Au sample and a W tip is used, the quantum efficiency drops to 10^{-6} or less (this is typically what was found in the experiments in Refs. 8 and 10). This estimate is found by noting that: (i) if the bias voltage is 2 V, in view of Eq. (27), less than 10 % of the area under the curves in Fig. 2 remains, and (ii) comparing Figs. 2 and 3 one realizes that the quantum efficiency for a Au-W configuration is about an order of magnitude smaller than for a Ag-Ir configuration.

Returning to Fig. 4 we see that the dissipated power is about 100 times as large as the radiated power; thus,

since about 2 out of 10^4 tunneling electrons take part in photon emission processes, it is clear that at most a few percent of all the electrons undergo some inelastic process while in the gap between the tip and sample. (The calculation of Ref. 27, using a two-sphere model geometry, showed that the inelastic current could account for up to 10 % of the total current.) In any case, the total tunnel current is dominated by the elastic part and the channels opened by inelastic processes only account for a rather small correction to the current. Most of the energy supplied by the bias voltage is eventually dissipated in hot-electron decay processes well inside the tip or sample.

These observations are important because our scheme for determining the tip-sample distance d that gives a certain tunnel current I at a certain bias voltage V_{bias} is now justified. In that calculation (see Ref. 22) we take $I = I_{\text{elastic}}$. *A priori*, nothing guarantees that the elastic contributions to the tunnel current are the dominating ones; given a sufficiently strong coupling to some other degrees of freedom, inelastic tunneling could dominate.

In the present case, the resistive losses into the tip (Ir) dominate for most frequencies; Ir is a rather bad conductor. However, just above 3.5 eV the losses into the sample are larger. This is mainly due to surface plasmon emission (the surface plasma frequency of silver is ≈ 3.7 eV). Then the tunneling electron excites a surface plasmon that can propagate quite far away from the tip-sample cavity, but eventually loses its energy due to dissipation into the sample.

Let us finally see what happens when *the tip and sample materials are interchanged*. Figure 5 compares the emission rates for a Ag sample-Ir tip with that of the combination Ir sample and Ag tip. In this calculation we used a “white” spectrum for the source.⁴⁴ As is seen, the magnitude of the emitted power can change by a factor of 2–3 as a result of the interchange in our model. Considering the details of the spectra there are further changes. The spectrum obtained with a Ag model tip has two peaks, and the one at higher frequency has the largest magnitude. Clearly, this peak originates, at least in part, from the fact that the model tip is a sphere, since it appears not very far below the frequency where an isolated silver sphere has a resonance.

C. Ag sample—Ag tip

The effects of retardation become even more apparent when we consider a situation in which both the tip and the sample are made of silver. Experiments have been done with tungsten tips covered by silver.⁴ The obtained spectra typically had two resonances. However, since the exact “composition” of the tip in these experiments is unknown, we will not calculate absolute intensities or make any comparison with experiment, but rather look at trends and make relative comparisons.

In Fig. 6, we display results for the radiation amplification factor, i.e. the actual differential power divided by the value it would take if the tip as well as the sample was absent, comparing the non-retarded and retarded calculations. Silver is a very good conductor over the entire frequency range up to $\hbar\omega=3.5$ eV, and tip-induced plasmons localized to the region around the tip-sample gap are very weakly damped, unless energy can be dissipated due to wave propagation. Therefore the spectrum resulting from a non-retarded calculation has a series of very sharp peaks. Once the finite speed of light is taken into account, these resonance peaks are broadened and their heights are reduced by about an order of magnitude. Still the amplification (enhancement) is very high. For example, if the corresponding curve was plotted for a Ag sample and an Ir tip, the peak value would be $\approx 10^5$. The changes brought about by including retardation can be understood by essentially the same reasoning as we used before.

In Fig. 7, we show how the differential power (calculated with a white power spectrum for the current⁴⁴) develops with increasing tip radius. Each spectrum has several, rather sharp peaks. The different resonances correspond to modes with different field distribution in the gap between the tip and the sample. The resonance with the lowest frequency is nodeless, the second peak comes from a mode that has one node, etc. As before, the resonances are red-shifted and broadened when R increases. As for the peak height, it first grows because a larger sphere functions as a larger “antenna” putting out more power. However, already at $R=300$ Å the peaks are lower and broader due to the increased damping. When this happens, the total radiated power remains approximately constant to begin with. But eventually also this trend is broken once the size of the sphere becomes comparable to λ ($\lambda/2\pi$). Then different parts of the sphere cannot send out radiation coherently any longer.

The differential power spectra are of course also sensitive to the tip-sample separation d . This is illustrated in Fig. 8. Keeping R fixed and increasing d , the resonances are shifted upwards in frequency due to a weaker coupling between the tip and sample. At the same time, the peak values decrease; with a larger tip-sample separation the field enhancement in the cavity becomes less effective, and the total photon yield decreases monotonically with increasing d . If one just looks at the intensity at a certain fixed photon energy, however, it can happen that the light intensity first increases as the tip approaches the surface, but then decreases again. This is due to the shift of the resonances as the tip-sample distance is changed; for a certain d a resonance appears at the frequency in question. An example of this is seen around $\hbar\omega = 2.1$ eV in Fig. 8.

In Fig. 9, we have plotted the total radiated and dissipated power calculated with a white power spectrum⁴⁴ for the current. There is a conspicuous peak in P_{sample} just above 3.5 eV, which is due to surface-plasmon excitation. However, over most of the rest of the frequency

range, the radiated power is comparable to P_{samp} and P_{sph} . Thus, in the present case, radiation damping really gives a significant contribution to the peak width.

D. Surface modifications to the dielectric response

As mentioned earlier, using dielectric functions determined from optical experiments is an approximation (however, as we will see, a good one) in the present problem. A more accurate dielectric function should include effects of extra damping due to surface scattering and electron-hole pair excitations. Here we will try to give an idea about the size of this damping using rather simple estimates.

To estimate the change in ϵ due to surface scattering, let us assume that the dielectric function at least over a certain frequency range can be written on the Drude form

$$\epsilon(\omega) = 1 - \left(\frac{\omega_p}{\omega}\right)^2 + i\frac{(\omega_p)^2}{\omega^3\tau}, \quad (28)$$

where ω_p is the plasma frequency, set by the density of conduction electrons, and τ is the electron mean free time. A simple estimate of τ is just $\tau = \ell/v_F$, where ℓ is a mean free path and v_F the Fermi velocity. Extra scattering off the surface should primarily occur in the tip, because it has of course a different shape than the flat surfaces used in the optical measurements in which the local dielectric functions were determined. But the standard tip materials Ir and W already have dielectric functions with large imaginary parts so an extra damping mechanism there makes no big difference. Let us therefore look at Ag, for which $\omega_p \approx 9\text{eV}$,⁴⁵ and $v_F \approx 1.4 \times 10^6$ m/s. With $\ell = 300$ Å (i.e. the tip radius we used most often) and $\hbar\omega = 2.5$ eV, we get an increase in $\text{Im}\epsilon$

$$\Delta(\text{Im}[\epsilon]) = \left(\frac{9}{2.5}\right)^2 \frac{1}{4.6 \times 10^{15}\text{s}^{-1} \times 2.1 \times 10^{-14}\text{s}} \approx 0.13. \quad (29)$$

In Fig. 10 we show how an extra contribution (here taken to be frequency-independent) to $\text{Im}\epsilon$ affects the radiation spectrum for a Ag-sample-Ir-tip combination. Extra damping leads to a decrease in the differential power, but the changes are still relatively small for realistic modifications (i.e., $\epsilon_{\text{Ag}} + i0.1$ and $\epsilon_{\text{Ag}} + i0.3$) of the dielectric function. Maybe the best justification for using optically measured dielectric functions is provided by a comparison between Figs. 3 and 10; changes in the tip geometry have larger effects than surface scattering.

Next we estimate the damping rate that result from the fact that a plasmon, which is a coherent superposition of electron-hole pair excitations, under certain circumstances can decay into real electron-hole pairs. To discuss this in a simple way, we will use the so called d-parameter theory of electromagnetic surface response of

a jellium.^{46–49} The frequency-dependent (and complex) function $d_{\perp}(\omega)$ tells where the centroid of the induced screening charge is situated relative to the jellium edge. The order of magnitude of d_{\perp} is set by k_F^{-1} , i.e. $d_{\perp} \sim 1$ Å. The surface response function of the jellium, $g(q_{\parallel}, \omega)$,⁵⁰ is modified (to lowest order in $q_{\parallel}d_{\perp}$) from its classical value $(\epsilon - 1)/(\epsilon + 1)$ to⁴⁶

$$g(q_{\parallel}, \omega) = \frac{\epsilon(\omega) - 1}{\epsilon(\omega) + 1} \left[1 + \frac{\epsilon(\omega)}{\epsilon(\omega) + 1} 2q_{\parallel}d_{\perp}(\omega) \right]. \quad (30)$$

Then, provided that q_{\parallel} is large enough that retardation effects can be neglected ($q_{\parallel} \gg \omega/c$) and using $\epsilon(\omega) = 1 - \omega_p^2/\omega^2$, the surface plasmon at an isolated jellium surface has the frequency

$$\omega = \omega_s \left[1 - q_{\parallel}d_{\perp}(\omega_s)/2 \right], \quad (31)$$

where the classical surface plasma frequency $\omega_s = \omega_p/\sqrt{2}$. Thus, for large enough q_{\parallel} , the resonance frequency will have a shift away from ω_s depending on $\text{Re} d_{\perp}$, and the damping of the surface plasmon depends on $\text{Im} d_{\perp}$. The analysis leading to Eq. (31) can be generalized to the situation where two jellium surfaces, a distance L apart, are facing each other. The resonance frequency for the low-frequency interface plasmon (from which the tip-induced mode illustrated in Fig. 1 can be derived) is given by

$$\omega_{\text{IP}} = \omega_s \sqrt{1 - e^{-q_{\parallel}L}} \left[1 - \frac{1 + e^{-q_{\parallel}L}}{1 - e^{-q_{\parallel}L}} \frac{q_{\parallel}d_{\perp}(\omega_{\text{IP}})}{2} \right], \quad (32)$$

if the two jellia are identical.

Let us apply this formula to the case of the tip-induced plasmon. Using the parameter values $\hbar\omega_{\text{IP}} = 2.5$ eV, $q_{\parallel} = \pi/100$ Å⁻¹ corresponding to a typical plasmon diameter (cf. Sec. II B), and $L = 5$ Å, we find that the electron-hole pair excitations will give an additional full-width-half-maximum broadening

$$\text{FWHM}_{\text{e-h pairs}} = -2\text{Im}[\hbar\omega_{\text{IP}}] \approx 0.15 \text{ eV}.$$

To get this value, we used

$$\text{Im} d_{\perp}(\omega/\omega_p = 0.3) \approx 0.16\text{Å},$$

as calculated by Liebsch⁴⁸ for $r_s = 3$ appropriate for silver. It is clear that the estimated FWHM is considerably smaller than the resonance peak widths found in Figs. 3 and 10.

V. CONCLUSIONS AND OUTLOOK

In this paper, we have presented a fully retarded calculation of the light emission rate from a scanning tunneling microscope probing a noble metal surface. The major aim was to investigate in what way, and to what

degree, the inclusion of retardation changed the results compared with our earlier non-retarded calculations.^{21,22}

In general, the results of the previous calculations still remain valid from a qualitative and semi-quantitative point of view. Light emission is resonantly enhanced due to the formation of a tip-induced plasmon mode in the cavity formed between the tip and sample. The enhancement amounts to 4 to 5 orders of magnitude compared with light emission in vacuum, and the quantum efficiency is typically 10^{-4} photons per tunneling electron. The resonant photon energy is ≈ 2.1 eV for Au samples and ≈ 2.0 eV for Cu samples, i.e., essentially the same results as were found before. In the case of Ag samples, taking retardation into account lowers the resonant photon energy by a few tenths of eV.

Our results can also be compared with some earlier calculations addressing either SERS,³³ or light emission.²⁶ Note that this comparison is possible thanks to the reciprocity theorem.³⁹ The present results give spectra that are very similar to the ones obtained in Ref. 33. Also in terms of intensities, the two calculations give similar results. A direct comparison of the numbers is not possible; here the relevant quantity is the square of the field enhancement at one point in space, while in SERS one calculates the fourth power of the field enhancement averaged over a certain surface (a model sphere in Ref. 33).

The results of a previous retarded calculation by Madrazo, Nieto-Vesperinas, and Garcia²⁶ addressing light emission from an STM differ from ours on a couple of points: (i) MNVG find lower enhancement factors, 10^3 at most, while we get 10^4 (Au sample–W tip), 10^5 (Ag–Ir), or even 10^6 (Ag–Ag). With a Ag sample and a Ag tip, and *exactly the same* parameter values for photon frequency, observation angle, and tip radius, and with $d = 8$ Å, we get an enhancement that is about 50 times larger than that found by MNVG. Moreover, MNVG state that a major part of the enhancement (approximately a factor 100) originates from the artificial corrugation of the sample. An important reason for the lower enhancement appears to be their using a two-dimensional geometry; their model tip is a horizontal cylinder and not a sphere, so the concentration of the electric field to the “end” of the tip is much less accentuated in their calculation. (ii) MNVG also found that interchanging tip and sample materials changed the photon yield by as much as a factor of 20. They only found a considerable enhancement when the sample material is a noble metal. In the present calculation, interchanging tip and sample materials changed the photon yield by at most a factor 2–3 (cf. Fig. 5). Again, this shows that the electromagnetic tip-sample interaction only plays a minor role for the field enhancement within the model of MNVG, whereas it is paramount in our model.

The present theory can be extended in a number of ways. If the sample is covered by an overlayer, or the tip is covered by a spherical shell of a different material, the calculations can be carried through in essentially the same way after a few modifications have been

made. With some more effort it should also be possible to treat cases where the tip has a more complicated shape, like for instance, a spheroid. In principle also regularly corrugated or randomly rough sample surfaces could be treated within an extension of the present framework, but the amount of numerical computations would be considerably larger than now. Finally, a calculation that could really treat an extended tip (i.e. one that continues out towards a tip-holder) would be useful. This is, however, a more difficult problem than those mentioned before.

In addition to this, the experiments by Alvarado and co-workers on the polarization properties of the emitted light and its dependence on the surface and tip properties have raised some interesting questions. For example, when the direction of magnetization of a Co film is reversed, the degree of polarization of the emitted light can change by up to 20 %.¹⁷ For a magneto-optic effect, this is a very large number, and the effect could be important if it turns out that it can be used to study surface magnetism with good spatial resolution. (However, in a similar experiment on iron, Pierce *et al.*⁵¹ found essentially no light polarization due to magnetism.) The experimental results of Ref. 17 indicate that tip-sample interactions play a role also for this effect. The emitted light was more polarized in the tunneling regime (low bias) than in the field-emission regime. Moreover, it is possible that the shape of the tip is important in these experiments. A very high degree of polarization can be reached using an asymmetrically shaped tip on a non-magnetic surface.⁵²

In summary, we have shown that retardation does play a role in light emission from STM’s, but that the changes are not too big. Thus, theoretical studies of new, more complicated effects like the light emission from magnetic surfaces can very well be carried out neglecting retardation. Comparing our results with those of Ref. 26, we conclude that it is essential to retain a three-dimensional tip geometry in order to get an enhancement of the light emission rate that is comparable to those found in experiment.

ACKNOWLEDGMENTS

This research was supported by the Swedish Natural Science Research Council (NFR). I thank Peter Apell and Richard Berndt for useful discussions and comments.

APPENDIX:

In this appendix we give explicit expressions for the functions $f_l(\kappa)$, $g_l(\kappa)$, $S(\kappa)$, and s_l ; we also indicate how these expressions are derived.

To this end it is useful to express the Green's function of Eq. (8) in representations suitable for cylindrical and spherical coordinates. In cylindrical coordinates

$$G(\mathbf{r}, \mathbf{r}') = i \sum_{m=0}^{\infty} \frac{2 - \delta_{m,0}}{4\pi} \cos(m(\phi - \phi')) \times \int_0^{\infty} \kappa d\kappa \frac{J_m(\kappa\rho) J_m(\kappa\rho')}{\sqrt{k^2 - \kappa^2}} e^{i\sqrt{k^2 - \kappa^2}|z - z'|}, \quad (\text{A1})$$

and for spherical coordinates

$$G(\mathbf{r}, \mathbf{r}') = ik \sum_{l=0}^{\infty} j_l(kr^<) h_l(kr^>) \sum_{m=0}^l \frac{(2 - \delta_{m,0})(2l + 1)}{4\pi} \times \frac{(l - m)!}{(l + m)!} P_l^m(\cos\theta) P_l^m(\cos\theta') \cos(m(\phi - \phi')), \quad (\text{A2})$$

where $r^<(r^>)$ is the lesser (greater) of r and r' , and h_l is a spherical Hankel function. In addition, the integral

$$\int_0^{\pi} \sin\theta d\theta e^{i\sqrt{k^2 - \kappa^2}R \cos\theta} J_1(\kappa R \sin\theta) P_l^1(\cos\theta) = 2i^{l-1} P_l^1(\sqrt{1 - \kappa^2/k^2}) j_l(kR) \quad (\text{A3})$$

will be used repeatedly.

Let us begin by looking at the contributions to \mathbf{B} in Eq. (7) coming from the sample. From Eq. (6),

$$\mathbf{B}(\mathbf{r}') = \hat{\phi}' \int_0^{\infty} \kappa d\kappa B(\kappa) J_1(\kappa\rho') \quad (\text{A4})$$

at the sample surface. To calculate the electric field just outside the sample surface, we first evaluate the \mathbf{E} field *inside* the sample from

$$\mathbf{E} = \frac{ic}{\epsilon_1 k} \nabla \times \mathbf{B}, \quad (\text{A5})$$

and then use the fact that the tangential component of \mathbf{E} is continuous across the sample surface. This yields

$$-\frac{ik}{c} (\hat{n}' \times \mathbf{E}(\mathbf{r}')) = \frac{i}{\epsilon_1} \hat{\phi}' \int_0^{\infty} \kappa d\kappa B(\kappa) J_1(\kappa\rho') \sqrt{k_1^2 - \kappa^2} \quad (\text{A6})$$

at the sample surface. Inserting Eqs. (A4), (A6), and (A1) into (7) and carrying out the surface integral, we find that the sample surface contribution to $\mathbf{B}(\mathbf{r})$ everywhere in the vacuum region can be written

$$\mathbf{B}^{(s)}(\mathbf{r}) = \hat{\phi} \int_0^{\infty} \kappa d\kappa B(\kappa) J_1(\kappa\rho) e^{i\sqrt{k^2 - \kappa^2}(z - z_0)} \times \frac{1}{2} \left[1 - \frac{\sqrt{k_1^2 - \kappa^2}}{\epsilon_1 \sqrt{k^2 - \kappa^2}} \right]. \quad (\text{A7})$$

Comparing this with Eq. (10), it is immediately clear that

$$S(\kappa) = \frac{1}{2} \left[1 - \frac{\sqrt{k_1^2 - \kappa^2}}{\epsilon_1 \sqrt{k^2 - \kappa^2}} \right]. \quad (\text{A8})$$

Furthermore, by calculating the overlap at the spherical surface between $\mathbf{B}^{(s)}(\mathbf{r})$, as given by Eq. (A7), and $P_l^1(\cos\theta)$, one finds, with the aid of Eq. (A3), the plane-to-sphere coupling

$$f_l(\kappa) = \frac{2l + 1}{l(l + 1)} i^{l-1} S(\kappa) \times e^{i\sqrt{k^2 - \kappa^2}(d+R)} P_l^1 \left(\sqrt{1 - \kappa^2/k^2} \right) j_l(kR). \quad (\text{A9})$$

Note that if $\epsilon_1 = 1$ both $S(\kappa)$ and $f_l(\kappa)$ vanish.

Next, we apply the same methods to calculate the contributions to $\mathbf{B}(\mathbf{r})$ from the spherical surface. This yields

$$s_l = ikR h_l(kR) j_l(kR) \times \left(kR \frac{j_l'(kR)}{j_l(kR)} + 1 - \frac{1}{\epsilon_2} \left[k_2 R \frac{j_l'(k_2 R)}{j_l(k_2 R)} + 1 \right] \right) \quad (\text{A10})$$

for the sphere-sphere coupling, while

$$g_l(\kappa) = \frac{i^l R^2}{\sqrt{k^2 - \kappa^2}} e^{i\sqrt{k^2 - \kappa^2}(d+R)} P_l^1 \left(\sqrt{1 - \kappa^2/k^2} \right) \times \left(k \frac{j_l'(kR)}{j_l(kR)} + \frac{1}{R} - \frac{1}{\epsilon_2} \left[\frac{1}{R} + k_2 \frac{j_l'(k_2 R)}{j_l(k_2 R)} \right] \right) j_l(kR) \quad (\text{A11})$$

describes how the waves originating from the sphere propagate to the sample surface. In this case, $\epsilon_2 = 1$ causes s_l and $g_l(\kappa)$ to vanish.

* Electronic mail: epj@teor.fys.lu.se

¹ Light emission (with lower intensity) had earlier been observed from ordinary tunnel junctions, see J. Lambe and S. L. McCarthy, Phys. Rev. Lett. **37**, 923 (1976).

² J. K. Gimzewski, B. Reihl, J. H. Coombs, and R. R. Schlittler, Z. Phys. B **72**, 497 (1988).

³ J. K. Gimzewski, J. K. Sass, R. R. Schlittler, and J. Schott, Europhys. Lett. **8**, 435 (1989).

⁴ R. Berndt, J. K. Gimzewski, and P. Johansson, Phys. Rev. Lett. **67**, 3796 (1991); **71**, 3493 (1993).

⁵ R. Berndt and J. K. Gimzewski, Phys. Rev. B **48**, 4746 (1993).

⁶ R. Berndt, R. Gaisch, W. D. Schneider, J. K. Gimzewski, B. Reihl, R. R. Schlittler, and M. Tschudy, Phys. Rev. Lett. **74**, 102 (1995).

- ⁷ I. I. Smolyaninov, V. S. Edelman, and V. V. Zavyalov, Phys. Lett. A **158**, 337 (1991).
- ⁸ V. Sivel, R. Coratger, F. Ajustron, and J. Beauvillain, Phys. Rev. B **45**, 8634 (1992).
- ⁹ K. Ito, S. Ohyama, Y. Uehara, and S. Ushioda, Surf. Sci. **324**, 282 (1995).
- ¹⁰ T. Umeno, R. Nishitani, A. Kasuya, and Y. Nishina, Phys. Rev. B **54**, 13 499 (1996).
- ¹¹ P. Dumas, C. Strykh, I. V. Makarenko, and F. Salvan, Europhys. Lett. **40**, 447 (1997).
- ¹² D. L. Abraham, A. Veider, Ch. Schönenberger, H. P. Meier, D. J. Arent, and S. F. Alvarado, Appl. Phys. Lett. **56**, 1564 (1990).
- ¹³ S. F. Alvarado and Ph. Renaud, Phys. Rev. Lett. **68**, 1387 (1992).
- ¹⁴ L. Montelius, M.-E. Pistol, and L. Samuelson, Ultramicroscopy **42-44**, 210 (1992).
- ¹⁵ J. Lindahl, M.-E. Pistol, L. Montelius, and L. Samuelson, Appl. Phys. Lett. **68**, 60 (1996).
- ¹⁶ R. Berndt, R. Gaisch, J. K. Gimzewski, B. Reihl, R. R. Schlittler, W. D. Schneider, and M. Tschudy, Science **262**, 1425 (1993).
- ¹⁷ A. L. Vázquez de Parga and S. F. Alvarado, Phys. Rev. Lett. **72**, 3726 (1994).
- ¹⁸ J. K. Gimzewski, R. Berndt, and R. R. Schlittler, Ultramicroscopy **42-44**, 366 (1992).
- ¹⁹ M. Völcker, W. Krieger, and H. Walther, Phys. Rev. Lett. **66**, 1717 (1991).
- ²⁰ U. Ch. Fischer and D. W. Pohl, Phys. Rev. Lett. **62**, 458 (1989); M. Specht, J. D. Pedarnig, W. M. Heckl, and T. W. Hänsch, *ibid.* **68**, 476 (1992); C. Baur, B. Koslowski, R. Möller, and K. Dransfeld, in Ref. 30, pp. 325-331 (1993).
- ²¹ P. Johansson, R. Monreal, and P. Apell, Phys. Rev. B **42**, 9210 (1990).
- ²² P. Johansson and R. Monreal, Z. Phys. B **84**, 269 (1991).
- ²³ B. N. J. Persson and A. Baratoff, Phys. Rev. Lett. **68**, 3224 (1992).
- ²⁴ Y. Uehara, Y. Kimura, S. Ushioda, and K. Takeuchi, Jpn. J. Appl. Phys. **31**, 2465 (1992).
- ²⁵ W. Denk and D. W. Pohl, J. Vac. Sci. Technol. B **9**, 510 (1991).
- ²⁶ A. Madrazo, M. Nieto-Vesperinas, and N. Garcia, Phys. Rev. B **53**, 3654 (1996).
- ²⁷ A. Downes, M. E. Taylor, and M. E. Welland, Phys. Rev. B **57**, 6706 (1998).
- ²⁸ R. W. Rendell and D. J. Scalapino, Phys. Rev. B **24**, 3276 (1981).
- ²⁹ A. G. Malshukov, Physics Reports **194**, 343 (1990).
- ³⁰ *Near Field Optics*, Vol. 242, *NATO ASI Series E: Applied Sciences*, edited by D. W. Pohl and D. Courjon (Kluwer, Dordrecht, 1993).
- ³¹ *Near Field Optics*, in *Ultramicroscopy* **61**, Nos. 1-4, edited by M. Paesler and N. van Hulst (Elsevier, Amsterdam, 1995).
- ³² O. J. F. Martin, C. Girard, and A. Dereux, Phys. Rev. Lett. **74**, 526 (1995).
- ³³ T. Takemori, M. Inoue, and K. Ohtaka, J. Phys. Soc. Jpn. **56**, 1587 (1987).
- ³⁴ W. R. Holland and D. G. Hall, Phys. Rev. B **27**, 7765 (1983); T. L. Ferrell, *ibid.* **50**, 14 738 (1994); A. V. Shchegrov, I. V. Novikov, and A. A. Maradudin, Phys. Rev. Lett. **78**, 4269 (1997).
- ³⁵ For a review, see D. W. Pohl, in *Advances in Optical and Electron Microscopy* edited by C. J. R. Sheppard and T. Mulvey (Academic, London, 1991), Vol. 12, p. 243.
- ³⁶ M. Moskovits, Rev. Mod. Phys. **57**, 783 (1985).
- ³⁷ J. H. Weaver, C. Krafska, D. W. Lynch, and E. E. Koch, *Physik Daten* (Fachinformationszentrum, Karlsruhe, 1981), Nos. 18-1 and 18-2, gives a compilation of optical properties for a large number of metals. The data for silver are taken from C. J. Flaten and E. A. Stern, Phys. Rev. B **11**, 638 (1975).
- ³⁸ J. D. Jackson, *Classical Electrodynamics* (Wiley, New York, 1975), pp. 432-435. The full formula contains also a term proportional to $\hat{n}' \cdot \mathbf{B}(\mathbf{r}')$ which does not contribute here.
- ³⁹ L. D. Landau, E. M. Lifshitz, and L. P. Pitaevskii, *Electrodynamics of Continuous Media* (Pergamon, Oxford, 1984), 2nd ed., pp. 308-309. The reciprocity theorem states that the induced field as a result of a certain source is unchanged when the source and field points are interchanged.
- ⁴⁰ See A. Madrazo and M. Nieto-Vesperinas, J. Opt. Soc. Am. A **13**, 785 (1996), for a more extensive discussion of the calculational method.
- ⁴¹ J. D. Jackson [Ref. 38], footnotes on p. 392 and p. 758; J. M. Blatt and V. F. Weisskopf, *Theoretical Nuclear Physics* (Wiley, New York, 1952), Ch. XII.
- ⁴² T. Schimizu, K. Kobayashi, and M. Tsukada, Appl. Surf. Sci. **60/61**, 454 (1992), calculated a quantity corresponding to $|C|^2(\omega)$ for a Ag sample and a W tip from first principles. The results in general agree well with Eq. (27).
- ⁴³ R. Berndt, Ph. D. thesis, Universität Basel, (1992).
- ⁴⁴ To be precise, this means that we have used a source of the form in Eqs. (1) and (2), where $C = 1 \text{ A}/\text{Å}$ (and independent of the frequency) and $a = 5 \text{ Å}$. Thus, the different results of this paper obtained with a white-spectrum source can be compared with each other directly.
- ⁴⁵ This value is set by the density of conduction electrons, and describes the optical properties of Ag for $\hbar\omega \lesssim 2.5 \text{ eV}$ reasonably well. The experimental plasmon energy, 3.8 eV, is strongly influenced by interband transitions.
- ⁴⁶ P. J. Feibelman, Prog. Surf. Sci. **12**, 287 (1982).
- ⁴⁷ P. Apell, Phys. Scr. **24**, 795 (1981).
- ⁴⁸ A. Liebsch, Phys. Rev. B **36**, 7378 (1987).
- ⁴⁹ For a recent review, see W. Plummer, K.-D. Tsuei, and B.-O. Kim, Nuclear Instruments and Methods in Physics Research B **96**, 448 (1995).
- ⁵⁰ $g(q_{\parallel}, \omega)$ equals the ratio $-(\phi_{\text{ind}}/\phi_{\text{ext}})$ at the surface, where ϕ_{ext} and ϕ_{ind} are external and induced scalar potentials, respectively, varying as $e^{i\mathbf{q}_{\parallel} \cdot \mathbf{r}_{\parallel} - i\omega t}$, see B. N. J. Persson and S. Andersson, Phys. Rev. B **29**, 4382 (1984).
- ⁵¹ D. T. Pierce, A. Davies, J. A. Stroschio, and R. J. Celotta, Appl. Phys. A **66**, S403 (1998).
- ⁵² A. L. Vázquez de Parga and S. F. Alvarado, Europhys. Lett. **36**, 577 (1996).

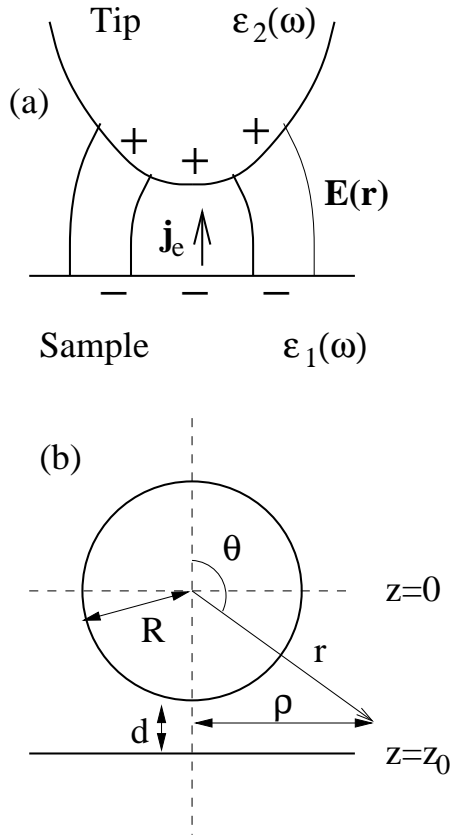


FIG. 1. Illustration of the tip-sample geometry (not to scale). In (a) the current \mathbf{j}_e exciting the system and the electric field associated with the tip-induced plasmon mode are shown. In (b) the model geometry and coordinate system employed in the calculations are shown.

$dP/d(\hbar\omega)d\Omega(10^6 \text{ s}^{-1})$

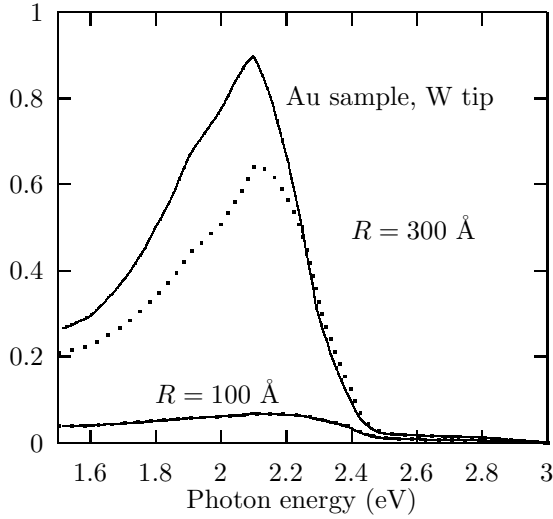


FIG. 2. Radiated power per unit solid angle and photon energy for the case of a gold sample and tungsten tip. The bias voltage is 3 V (negative sample) and the tunnel current is 10 nA. The corresponding tip-sample separation d was 5.71 Å ($R=100$ Å) and 6.30 Å ($R=300$ Å). The continuous curves show results of retarded calculations, while the dotted curves show results calculated without accounting for retardation.

$dP/d(\hbar\omega)d\Omega(10^6 \text{ s}^{-1})$

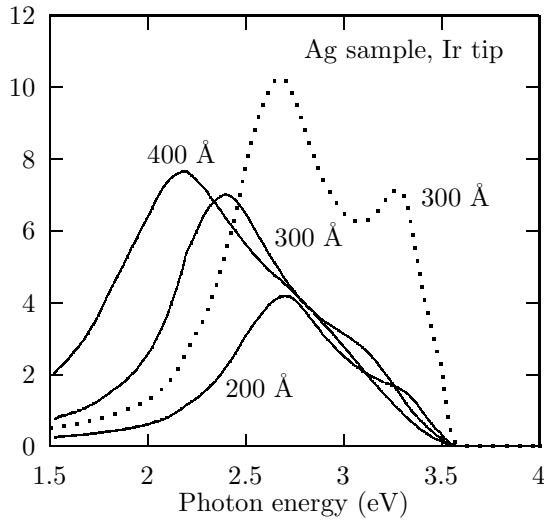


FIG. 3. Radiated power per unit solid angle and photon energy with a silver sample and iridium tip. The bias voltage is 4 V, the current is 10 nA, and the corresponding tip-sample separations are: $d=6.09 \text{ \AA}$ (for $R=200 \text{ \AA}$), $d=6.28 \text{ \AA}$ ($R=300 \text{ \AA}$), and $d=6.41 \text{ \AA}$ ($R=400 \text{ \AA}$). As in Fig. 2, the continuous (dotted) curve shows results from a retarded (non-retarded) calculation.

Total power (10^6 s^{-1})

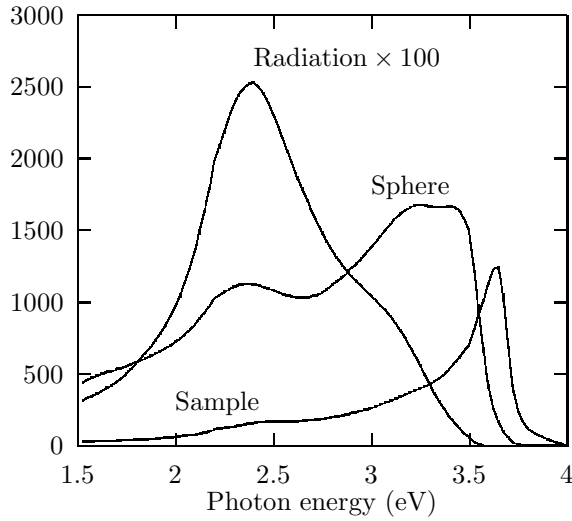


FIG. 4. The total power per unit photon energy emitted as radiation, and dissipated into the tip and sample. The calculation takes retardation into account. The tip and sample materials are Ir and Ag, respectively, the tip radius $R=300 \text{ \AA}$, and the rest of the parameter values are the same as in Fig. 3. To facilitate direct comparison, the radiation power data have been multiplied by a factor of 100.

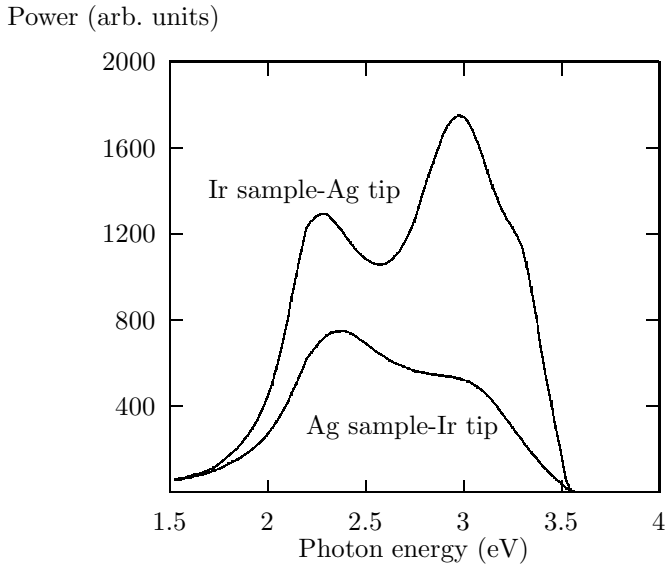


FIG. 5. Effects of interchanging tip and sample materials. The two curves show the calculated differential power, given that the driving current has a white spectrum.⁴⁴

Amplification factor

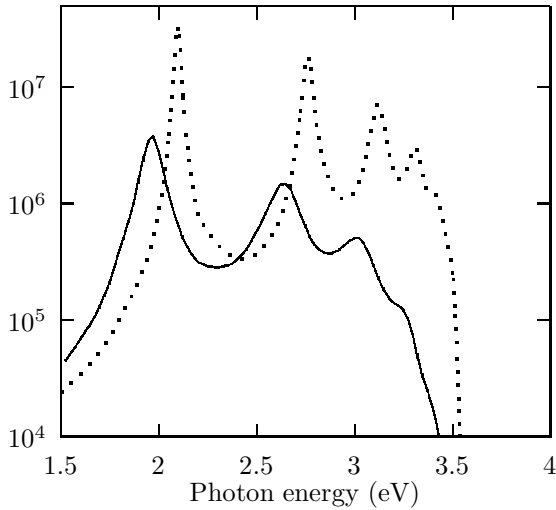


FIG. 6. Radiation amplification factor for an Ag sample and Ag tip with $R=300 \text{ \AA}$ and $d=5 \text{ \AA}$. The amplification factor is the ratio between the radiated differential power with tip and sample present, and the radiated power into vacuum given the same source distribution. The dotted curve gives the results from a non-retarded calculation. The peaks of this curve are about 10 times higher and sharper than those of the continuous curve resulting from a retarded calculation. Note the logarithmic scale.

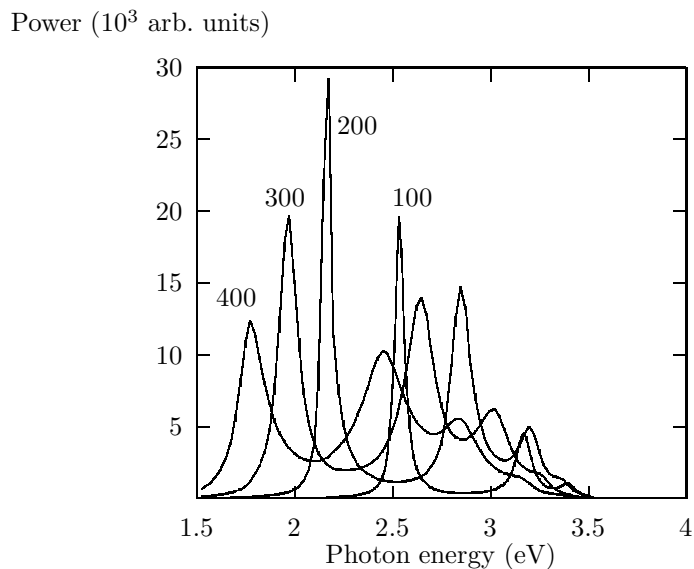


FIG. 7. Results for the differential power for the case of a Ag sample and Ag tip. A white power spectrum⁴⁴ was used for the current driving the light emission. The calculations were done taking retardation into account. The tip radii were 100, 200, 300, and 400 Å, respectively, as indicated next to the curves, and $d=5$ Å.

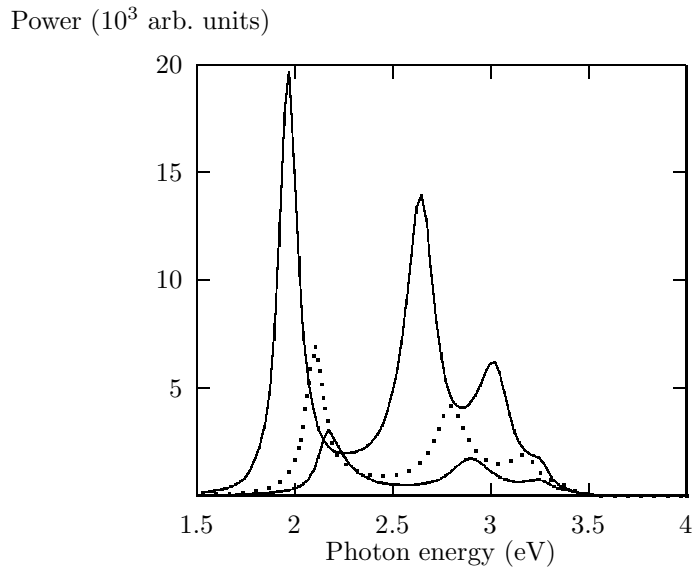


FIG. 8. Differential power (calculated with a white spectrum⁴⁴ for the driving current) for a Ag sample and Ag tip with $R=300$ Å for varying tip-sample distance. $d=5$ Å for the curve with highest peaks, $d=7.5$ Å for the dotted curve, and $d=10$ Å for the curve showing the lowest intensity.

Power (10^6 arb. units)

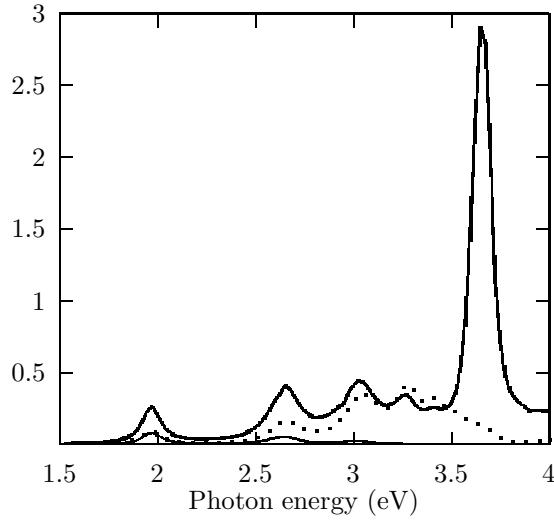


FIG. 9. Total radiated, and dissipated power per unit photon energy for a Ag sample and Ag tip ($R=300$ Å and $d=5$ Å). The thin curve gives the total radiated power, the other curves show the dissipated power into the sample (thick curve) and tip (dotted curve). The results were calculated with a white spectrum⁴⁴ for the current.

Power (arb. units)

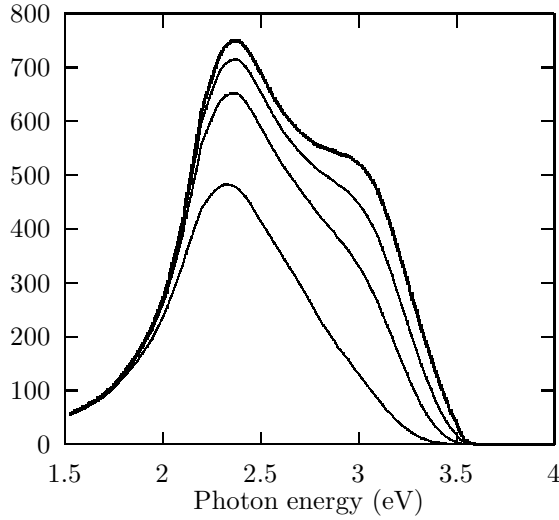


FIG. 10. Differential power (calculated with a white spectrum⁴⁴ for the driving current) for a Ag sample and Ir tip with $R=300$ Å and $d=5$ Å. The different curves show how the spectrum develops as the imaginary part of the Ag dielectric function is increased: The thick curve gives the result obtained with ϵ_{Ag} determined from optical experiments. The remaining curves were calculated using $\epsilon_{Ag} + i0.1$, $\epsilon_{Ag} + i0.3$, and $\epsilon_{Ag} + i1.0$, respectively.